A Bayesian approach for energy-based estimation of acoustic aberrations in high intensity focused ultrasound treatment[*]

Bamdad Hosseini [†], Charles Mougenot [‡], Samuel Pichardo [§], Elodie Constanciel [¶], James M. Drake [¶], and John M. Stockie [†]

Abstract. High intensity focused ultrasound is a non-invasive method for treatment of diseased tissue that uses a beam of ultrasound in order to generate heat within a small volume. A common challenge in application of this technique is that heterogeneity of the biological medium can defocus the ultrasound beam. In this study, the problem of refocusing the beam is reduced to the Bayesian inverse problem of estimating the acoustic aberration due to the biological tissue from acoustic radiative force imaging data. The solution to this problem is a posterior probability density on the aberration which is sampled using a Metropolis-within-Gibbs algorithm. The framework is tested using both a synthetic and experimental dataset. This new approach has the ability to obtain a good estimate of the aberrations from a small dataset, as little as 32 sonication tests, which can lead to significant speedup in the treatment process. Furthermore, this framework is very flexible and can work with a wide range of sonication tests and so it can be used alongside existing energy-based techniques.

Key words. Focused ultrasound, inverse problem, Bayesian, Parameter estimation.

AMS subject classifications. 92C55, 15A29, 62F15.

1. Introduction. High intensity focused ultrasound (HIFU) treatment is a non-invasive method for treatment of diseased tissue. The treatment uses a focused beam of ultrasound waves that converge onto a focal point. The resulting absorption of ultrasound generates heat which in turn can ablate the targeted tissue. The method has shown clinical success in treatment of uterine fibroids [14, 19, 38], prostate cancer [10], liver tumours [20, 43], brain disorders [13] and other medical conditions [21, 26, 27]. However, application of this method for treatment of brain tissue remains a challenge. Strong aberrations due to the skull bone, specifically the shift in the phase of the acoustic signal, defocus the beam and result in a loss of acoustic pressure. One approach for resolving this problem is to estimate the introduced acoustic aberrations. If the estimate is accurate enough then one can compensate the phase of the acoustic signals (at the transducer) and refocus the beam behind the skull bone.

One approach for estimating the aberrations is to use Magnetic Resonance (MR) imaging [17] or Computed Tomography (CT) [3, 30] in order to obtain a three dimensional model of the patient's skull and use this information in a computer model to estimate the tissue aberration and find the needed phase shift in order to refocus the beam. However, this approach is

---

[†]Department of Mathematics, Simon Fraser University, 8888 University Drive, Burnaby, BC, V5A 1S6, Canada (bhossein@sfu.ca, jstockie@sfu.ca)

[‡]Philips Healthcare, 281 Hillmount Road, Markham, ON, L6C 2S3, Canada (charles.mougenot@philips.com)

[§]Thunder Bay Regional Research Institute, Thunder Bay, ON, P7B 6V4, Canada (spichard@lakeheadu.ca)

[¶]Hospital for Sick Children, 555 University Avenue, Toronto, ON, M5G 1X8, Canada (elodie.constanciel@sickkids.ca, james.drake@sickkids.ca)

limited by both the computational cost of the model and the accuracy of the estimates for the acoustic properties of the tissues.

An alternative approach is the so called energy-based focusing techniques of [16, 25]. Here, Magnetic Resonance Acoustic Radiation Force Imaging (MR-ARFI) is used to obtain measurements of the intensity of the acoustic field at the focal point. MR-ARFI uses low-duty cycle HIFU pulses that generate tissue displacement in the order of microns at the focal point of the beam. The small displacement is measured with MRI using gradient pulses that encode the tissue displacement in the phase information of an MR image [7, 32]. Using ARFI, displacement maps are generated and can be used to verify and correct the degree of focusing of HIFU beam [31]. The energy-based focusing techniques in [16, 25] use a dataset of displacement maps that is generated by imposing specific excitation patterns at the ultrasound transducer. Columns of a Hadamard matrix are used for generating the excitation patterns in [16] while [24] uses Zernink polynomials. Afterwards, the resulting displacement maps are used to estimate both the acoustic field of the transducer and the aberrations induced by the ultrasound propagation medium. The main drawback of this technique is the need for a large number of sonication tests which requires a long acquisition time for the MRI data. Recently, it was argued in [29] that energy-based techniques can be cast as a penalized least-squares problem which enables one to use more general excitation patterns. They showed that using randomized calibration sequences can reduce the number of sonication tests significantly.

This article demonstrates the feasibility of using a new Bayesian method to estimate the acoustic aberrations with a small number of sonication tests. The central idea is to cast this problem within the framework of Bayesian inverse problems. The Bayesian perspective provides a general framework for estimation of parameters that model the aberrations from a finite set of measurements. Appropriate models are chosen to explain the data, the measurement noise and prior knowledge of the parameters. Afterwards, an entire probability distribution on the parameters is at hand rather than finding a single point estimator. The Bayesian formulation can be viewed as a generalization of the least-squares formulation of [29] (mini-mizers of penalized least-squares functionals are often equivalent to maximizers of the density of an underlying posterior distribution when the parameters are finite dimensional [22]). This allows for stable estimation of the aberrations with very noisy data and few sonication tests. Furthermore, this approach provides an estimate of the true value of the parameters as well as the associated uncertainties in that estimate. An introduction to the Bayesian perspective for solution of inverse problems and many of the techniques that are used in this article can be found in the monographs [4, 22, 40] and the article [39] as well as the references therein. The Bayesian approach to inverse problems has been successfully applied in various areas of medical imaging such as electrical impedance tomography [23], optical diffuse tomography [2] and dynamic X-ray tomography [33] as well as other fields such as astronomy [12, 35] and geoscience [11, 18, 40].

In this article, a farfield approximation to the three dimensional acoustic equation is used as a forward model that can be evaluated efficiently. Then, the effect of the tissue is mod-elled as an infinitely thin aberrator in front of the transducer, following [29]. Afterwards, a hierarchical smoothness prior is constructed that reflects the prior knowledge that the aber-ration parameters tend to change smoothly between nearby elements on the transducer, i.e. the properties of the tissue do not change dramatically between the elements. Combining

this prior knowledge with the forward model and the data, results in a posterior distribution which is viewed as the solution to the inverse problem. A Metropolis-within-Gibbs (MwG) sampler [28, 37] is used for exploring this distribution and obtaining several statistics such as the posterior mean and standard deviation of the aberrations as well as independent samples. Finally, we consider the posterior mean to be a good point-wise estimator of the parameters.

The remainder of this article is organized as follows. Section 2 is dedicated to the mathematical theory and the setup of the problem. A brief introduction to the farfield approximation of the acoustic equation is presented which is followed by the setup of the forward model that explains the MR-ARFI data. Next, the formulation of the Bayesian inverse problem is discussed where the likelihood and prior distributions are constructed. At the end of this section a MwG algorithm for sampling the posterior distribution is proposed. Section 3 concerns the setup of the test for synthetic and experimental conditions that were performed to verify the efficiency of the method. The results are then presented in Section 4 which is followed by a discussion of the mathematical framework and the results in Section 5.
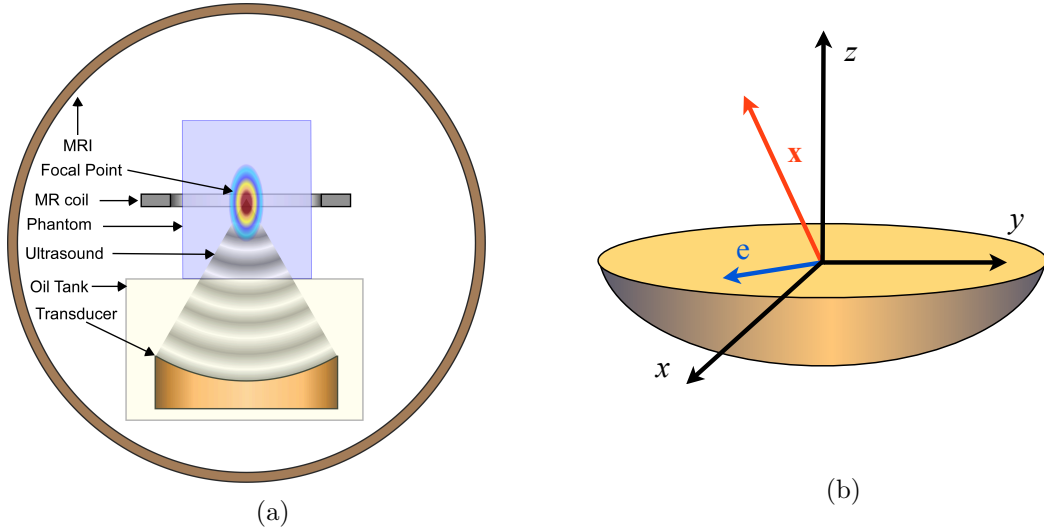

(a)

(b)

Figure 1.1: (a) Schematics of the high intensity focused ultrasound setup. The transducer is submerged in an oil tank and generates an acoustic field which is directed at a phantom. The resulting displacements are measured using an MR-coil inside an MRI machine. (b) The coordinate system of the transducer that is used in equations (2.1)–(2.3) for computing the acoustic field.

1.1. Notation. Throughout this article lower case and greek bold letters denote vectors and upper case bold letters denote matrices. Given a matrix $\mathbf{A}$ we use $\mathbf{A}^*$ to denote its adjoint. Finally, given $\mathbf{m} \in \mathbb{R}^N$ and a positive definite matrix $\mathbf{\Sigma} \in \mathbb{R}^{N \times N}$, we use $\mathcal{N}(\mathbf{m}, \mathbf{\Sigma})$ to denote a Gaussian random variable with mean $\mathbf{m}$ and covariance matrix $\mathbf{\Sigma}$.

2. Mathematical background and theory.

2.1. Forward problem.

A farfield approximation to the acoustic field of a single piezoelectric ultrasound element is obtained using the Rayleigh integral [36]. The ultrasound transducer consists of elements that are smaller in size than the wavelength. Each element emits an acoustic wave of amplitude p_0 [Pa] and frequency ω [Hz]. The pressure field $p(\mathbf{x})$ [Pa] at a location $\mathbf{x}$ [m], generated by a piezoelectric element at location $\mathbf{e}$ [m] (see Figure 1.1) is given by

$$p(\mathbf{x}; \mathbf{e}) = zf(\mathbf{x}; \mathbf{e}) \quad \text{where} \quad z = p_0 \exp(i\omega t) \quad \text{and} \quad f(\mathbf{x}; \mathbf{e}) = \exp\left(i\frac{\omega}{c_0}|\mathbf{x} - \mathbf{e}|\right). \qquad (2.1)$$

Here c_0 [m/s] is the speed of sound and $f(\mathbf{x}; \mathbf{e})$ is referred to as the free-field of the element [29]. Interaction of the acoustic waves with the tissue results in dissipation of energy and a shift in the phase as a result of friction (micro-scale displacements) and scattering [41]. The acoustic pressure $\tilde{p}(\mathbf{x})$ in the presence of the tissue can be modelled as

$$\tilde{p}(\mathbf{x}; \mathbf{e}) = \mu p(\mathbf{x}; \mathbf{e}) \quad \text{where} \quad \mu = \zeta \exp(i\phi t). \qquad (2.2)$$

Here, ζ is the attenuation coefficient (damping ratio of the amplitude) and ϕ is the shift in phase.

The acoustic field of the entire emitter can be obtained by summing the acoustic field of the individual piezoelectric elements. Let N denote the number of piezoelectric elements ($N = 256$ in the case of the Philips Sonalleve V1 system (Philips, Healthcare, Vantaa, Finland) that is used in the experiments of Section 3.2) and let $\mathbf{z} \in \mathbb{C}^N$ denote the sonication pattern at the transducer which is the vector containing the phase and amplitude of each element. Also, $\mathbf{a} \in \mathbb{C}^N$ is defined as the vector of aberrations pertaining to each element (the μ variable in (2.2)). Finally, define the field of view to be the displacement data of a region of $\sqrt{M} \times \sqrt{M}$ voxels around the focal point which is extracted from MR-ARFI images ($\sqrt{M} = 19$ in Section 4 for the synthetic test and $\sqrt{M} = 7$ for the physical experiment). Let $\tilde{\mathbf{p}} \in \mathbb{C}^M$ denote the measured values of the pressure at each voxel in presence of aberrations concatenated into a long vector. Then

$$\tilde{\mathbf{p}} = \tilde{\mathbf{F}} \, \text{diag}(\tilde{\mathbf{z}})\mathbf{a}, \qquad (2.3)$$

where $\text{diag}(\tilde{\mathbf{z}})$ is the diagonal matrix created from the elements of $\tilde{\mathbf{z}}$ and $\tilde{\mathbf{F}} \in \mathbb{C}^{M \times N}$ is referred to as the free-field matrix [29] which is the mapping of the pressure in the absence of aberrations. This model relies on the assumption that tissue aberrations can be modelled as an infinitesimally thin aberrator in front of the transducer [29]. The measured displacement in MR-ARFI images is proportional to the total intensity of the signal which is equal to the square of the modulus of pressure [32]. The constant of proportionality is generally unknown but it can be estimated in a calibration step as discussed in Section 3.2.1. Throughout the remainder of this article the constant of proportionality is accounted for in the free-field matrix. To this end, let $\tilde{\mathbf{d}} \in \mathbb{R}^M$ be the vector of displacements at each voxel. Then

$$\tilde{\mathbf{d}} = \text{diag}(\tilde{\mathbf{p}})\tilde{\mathbf{p}}^* \qquad (2.4)$$

where $\tilde{\mathbf{p}}^*$ denotes the element by element complex conjugate of $\tilde{\mathbf{p}}$. In practice, a finite number of J sonication tests are performed where vectors $\tilde{\mathbf{z}}_j$ for $j = 1, \cdots, J$ are prescribed as input at the transducer and give rise to MR-ARFI images. Each image can be summarized as a

vector of displacements $\tilde{\mathbf{d}}_j$. These measurements constitute a dataset that is used to estimate the aberrations $\mathbf{a}$. Then, a model is needed in order to relate $\mathbf{a}$ to the entire displacement dataset. Define the matrices

$$
\mathbf{Z} := \begin{bmatrix} \operatorname{diag}(\tilde{\mathbf{z}}_1) \\ \operatorname{diag}(\tilde{\mathbf{z}}_2) \\ \vdots \\ \operatorname{diag}(\tilde{\mathbf{z}}_J) \end{bmatrix} \in \mathbb{C}^{JN \times N}, \qquad \mathbf{F} := \mathbf{I}_{J \times J} \otimes \tilde{\mathbf{F}} \in \mathbb{C}^{JM \times JN},
$$

$$
\mathbf{p} := \begin{bmatrix} \tilde{\mathbf{p}}_1 \\ \tilde{\mathbf{p}}_2 \\ \vdots \\ \tilde{\mathbf{p}}_J \end{bmatrix} \in \mathbb{C}^{JM}, \qquad \mathbf{d} := \begin{bmatrix} \tilde{\mathbf{d}}_1 \\ \tilde{\mathbf{d}}_2 \\ \vdots \\ \tilde{\mathbf{d}}_J \end{bmatrix} \in \mathbb{R}^{JM},
$$

(2.5)

where $\mathbf{I}_{J \times J}$ is the $J \times J$ identity matrix and $\otimes$ denotes the usual Kronecker product. Then the forward model can be written as

$$
\mathbf{d} = \operatorname{diag}(\mathbf{p})\mathbf{p}^* \quad \text{where} \quad \mathbf{p} = \mathbf{FZa}. \tag{2.6}
$$

2.1.1. Relaxation to a continuous field. Figure 2.1 shows examples of phase shift and attenuation obtained with hydrophone measurements for a newborn skull using the Philips Sonalleve V1 system [8]. A schematic of the setup is depicted in Figure 2.1(a) and each image (Figures 2.1(b-d)) shows the measured phase shift and attenuation per transducer element mapped on a 2D projection of the transducer for a different orientation of the skull. The aberrations appear to change smoothly between the elements due to the presence of a soft spot in the skull sample. This suggests that a continuous function is a good model for the aberrations.

The acoustic elements on the emitter are arranged on a segment of a sphere (see Figure 1.1). Project the location of the elements on the xy-plane and assume that the pair $\{\bar{\mathbf{x}}, \bar{\mathbf{y}}\}$ are vectors of the normalized x and y coordinates of the elements so that all of the points fit within the unit disk in $\mathbb{R}^2$. Furthermore, let $[-1,1]^2$ denote the centred unit square in 2D and consider a function $a : [-1,1]^2 \to \mathbb{C}$ that is continuous. Next, define the continuous linear operator

$$
S : C([-1,1]^2) \to \mathbb{C}^N \quad (S(a; \bar{\mathbf{x}}, \bar{\mathbf{y}}))_j := a(\bar{x}_j, \bar{y}_j),
$$

for $a \in C([-1,1]^2)$ and $j = 1, \cdots, N$. Combining this with (2.6) defines the forward model for a continuous aberration function:

$$
\mathbf{d} = \mathcal{G}(a), \qquad \mathcal{G} : C([-1,1]^2) \to \mathbb{R}^{JM} \qquad \mathcal{G}(a) := \operatorname{diag}(\mathbf{FZ}S(a))(\mathbf{FZ}S(a))^*, \tag{2.7}
$$

where the dependence of S on the coordinate vectors is suppressed because the entries are fixed parameters that only depend on the geometry of the device.

2.2. Inverse problem. The key component of the Bayesian approach to inverse problems is the Bayes rule which can be written (informally) as

$$
\pi_{\text{post}}(a|\mathbf{d}_{\text{obs}}) \propto \pi_{\text{likelihood}}(\mathbf{d}_{\text{obs}}|a)\pi_{\text{prior}}(a) \tag{2.8}
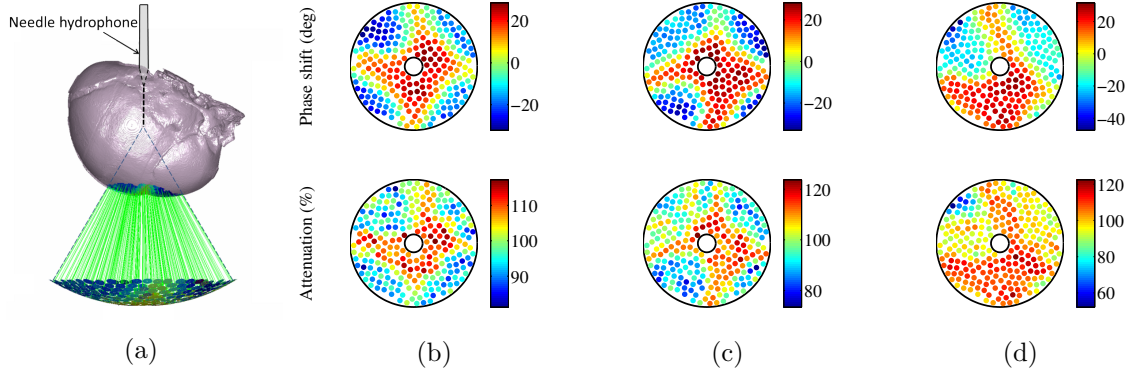$$

Figure 2.1: (a) The setup for hydrophone measurements. (b-d) Examples of attenuation (top) and phase shift (bottom) of the ultrasound elements measured at different areas of a newborn skull [8]. The aberration changes smoothly between the elements, which motivates the assumption that the aberrations can be modelled as a continuous function.

where π_{prior} is the *prior* probability distribution, reflecting prior knowledge about the parameter a, $\pi_{\text{likelihood}}$ is the *likelihood* distribution, indicating the chance of an observed dataset assuming that the parameter a was known, and π_{post} is the *posterior* distribution which is the updated distribution on a given both the data and the prior. In order to avoid the delicacy of setting up the Bayesian inverse problem on the function space we only consider the discretized version of the problem where the probability distributions have well-defined Lebesgue densities and refer the reader to [39] for a detailed discussion on this subject.

2.2.1. Likelihood distribution $\pi_{\text{likelihood}}$. Note that the forward model in (2.7) does not incorporate measurement errors and therefore is not a complete model of the observed data. Assume that the error between the prediction of the forward model and the observed data, denoted by $\mathbf{d}_{\text{obs}}$, can be modelled as an independent Gaussian random variable. Then

$$\mathbf{d}_{\text{obs}} = \mathcal{G}(a) + \boldsymbol{\eta} \qquad \text{where} \qquad \boldsymbol{\eta} \sim \mathcal{N}(0, \boldsymbol{\Sigma}), \tag{2.9}$$

where $\boldsymbol{\eta}$ is the measurement error and $\boldsymbol{\Sigma}$ is a positive definite matrix representing the covariance of the error. The random variable $\boldsymbol{\eta}$ has a density with respect to the Lebesgue measure in $\mathbb{R}^{JM}$

$$\pi_{\boldsymbol{\eta}}(\mathbf{x}) = (2\pi)^{-\frac{JM}{2}} |\Sigma|^{-\frac{1}{2}} \exp\left(-\frac{1}{2}\mathbf{x}^*\boldsymbol{\Sigma}^{-1}\mathbf{x}\right). \tag{2.10}$$

The conditional distribution of the observed data for a fixed a, which is simply the likelihood, is given as

$$\pi_{\text{likelihood}}(\mathbf{d}_{\text{obs}}|a) = \pi_{\boldsymbol{\eta}}(\mathbf{d}_{\text{obs}} - \mathcal{G}(a)) = \frac{1}{\beta}\exp(-\Phi(a; \mathbf{d}_{\text{obs}})), \tag{2.11}$$

where

$$\Phi(a; \mathbf{d}_{\text{obs}}) := \frac{1}{2}\left(\mathcal{G}(a) - \mathbf{d}_{\text{obs}}\right)^* \boldsymbol{\Sigma}^{-1}\left(\mathcal{G}(a) - \mathbf{d}_{\text{obs}}\right) \tag{2.12}$$

is referred to as the *likelihood potential* and $\beta := (2\pi)^{-JM/2}|\mathbf{\Sigma}|^{-1/2}$ is the normalizing constant so that $\pi_{\text{likelihood}}$ is a proper probability distribution.

2.2.2. Hierarchical prior distribution π_{prior}.

Recall that the function a was defined on the unit square $[-1, 1]^2$. Now suppose that the box is discretized using a uniform grid of size h and define the matrix $(\mathbf{A})_{jk} := a(-1 + (j-1)h, -1 + (k-1)h)$ for $j, k = 1, 2, \cdots, \sqrt{G}$ and $\sqrt{G} = 2/h + 1$, which is the usual finite difference discretization of a (see Figure 2.2(a)). Now, take $\mathbf{a}_h \in \mathbb{C}^G$ to be the vector that is obtained by concatenating the entries of $\mathbf{A}$ column by column and define the matrices

$$\tilde{\mathbf{L}} := \frac{1}{h^2} \begin{bmatrix} 2 & -2 & 0 & \cdots & \cdots & 0 \\ -1 & 2 & -1 & \cdots & \cdots & 0 \\ \vdots & \vdots & & & & \vdots \\ 0 & \cdots & \cdots & -1 & 2 & -1 \\ 0 & \cdots & \cdots & & -2 & 2 \end{bmatrix} \in \mathbb{R}^{\sqrt{G} \times \sqrt{G}} \quad \text{and} \quad \mathbf{L} := \tilde{\mathbf{L}} \otimes \tilde{\mathbf{L}} \in \mathbb{R}^{G \times G}. \quad (2.13)$$

The hierarchical prior distribution is constructed by first introducing the random variables

$$\mathbf{u} \sim \mathcal{N}(0, \mathbf{P}^{-1}), \quad \mathbf{v} \sim \mathcal{N}(0, \mathbf{P}^{-1}), \quad \alpha_1 \sim \mathcal{N}(0, \sigma_1^2), \quad \alpha_2 \sim \mathcal{N}(0, \sigma_2^2) \quad (2.14)$$

where $\mathbf{P} := h(\mathbf{I}_{G \times G} - \gamma \mathbf{L})^2$ and σ_1 and σ_2 are fixed. Then the prior on the aberration is represented via the random variable

$$\mathbf{a}_h \sim \pi_{\text{prior}}, \quad \mathbf{a}_h = \mathbf{a}_h(\boldsymbol{\theta}) := \text{diag}(\bar{\mathbf{u}} + \alpha_1^2 \mathbf{u}) \exp(i(\alpha_2^2 \mathbf{v})), \quad \boldsymbol{\theta} := \begin{bmatrix} \alpha_1 & \alpha_2 & \mathbf{u}^* & \mathbf{v}^* \end{bmatrix}. \quad (2.15)$$

Here, $\bar{\mathbf{u}}$ is the prior mean of the attenuation which is introduced separately since it is fixed, the exponential function is applied element by element and $\boldsymbol{\theta}$ is introduced to simplify notation in the next section.

The $\mathbf{P}^{-1}$ covariance operator in (2.14) is a finite difference discretization of the biharmonic operator $(I - \gamma \Delta)^{-2}$ with homogeneous Neumann boundary conditions. Here, Δ is the Laplacian in 2D. The finite difference matrix is scaled by a factor h so that draws from the prior have the proper white noise scaling in the continuum limit as $h \to 0$. The parameter γ controls the size of the features in the samples. Figure 2.2(b) shows a few samples of $\mathcal{N}(0, \mathbf{P}^{-1})$ for different values of γ discretized on a 50×50 grid (i.e. $G = 50^2$).

We refer to α_1 and α_2 as hyperparameters. They control the variance of the samples, indicating prior knowledge of the range of variations of the phase shift or attenuation. Introducing the hyperparameters as multipliers is crucial to making sure that the sampling algorithm in the next section is well defined in the continuum limit [1].

It is known that in the continuum limit, draws from the Gaussian distributions in (2.14) are almost surely Lipschitz continuous [39, Lemma 6.25]. Therefore, (2.15) serves as a good model for the aberrators of Figure 2.1. Since the samples are continuous, a straight forward linear interpolation can be used to obtain point values of the samples at the location of the elements. Therefore, the S operator of (2.7) is easily approximated with an interpolation matrix $\mathbf{S}$.
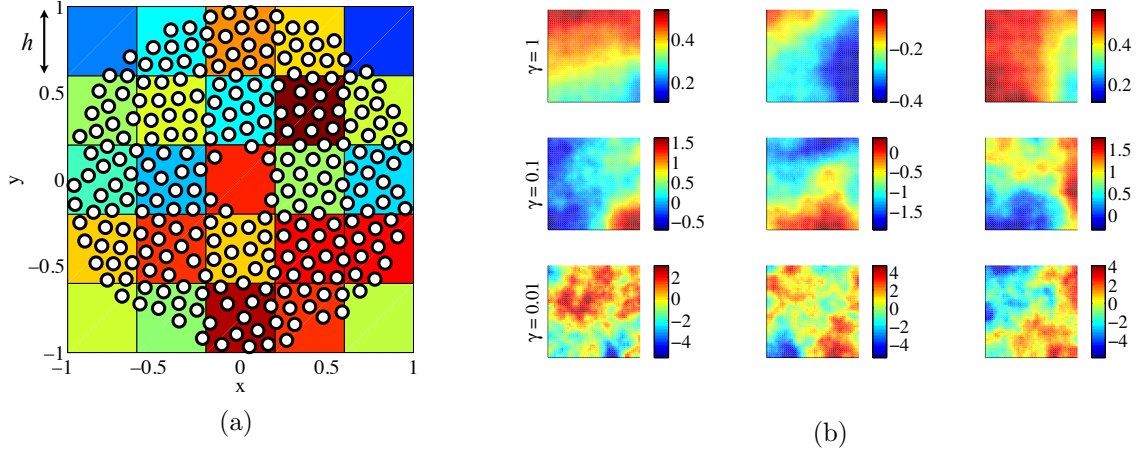
(a)

(b)

Figure 2.2: (a) Schematic of the underlying field a discretized on a uniform grid of size h. The value of the field is interpolated up to each element of the transducer using a simple interpolation matrix. (b) Examples of draws from the Gaussian distribution $\mathcal{N}(0, \mathbf{P}^{-1})$ for various values of γ on a 50×50 grid. Smaller values of γ result in samples with smaller features and larger amplitudes.

2.3. Sampling the posterior distribution π_{post}. The posterior distribution π_{post} is, in essence, the solution to the inverse problem. However, representing this distribution is infeasible in practice since it may not have a closed form. Therefore, one often tries to extract different statistics of this distribution or simply obtain independent samples from it.

Equations (2.11) and (2.15) identify π_{post} via (2.8) up to a normalizing constant. Computing this constant is often infeasible. However, Markov Chain Monte Carlo (MCMC) methods can still be used to generate samples from π_{post} without knowledge of this normalizing constant [37]. In this article, the preconditioned Crank-Nicolson (pCN) and Metropolis-Adjusted Langevin (MALA) algorithms of [9] are used in a Metropolis within Gibbs (MwG) sampler to generate samples from π_{post}. Here, the MALA algorithm is used to sample from $\mathbf{u}$ and α_1 and pCN is used to sample from $\mathbf{v}$ and α_2. The reason for this choice is the fact that the forward map (2.7) is not differentiable with respect to the phase and so the pCN algorithm is utilized to sample in this direction. The resulting algorithm can be summarized as follows:

Metropolis within Gibbs (MwG) sampler.

1. Set $k = 0$ and choose $\boldsymbol{\theta}^{(0)}$ by picking $\mathbf{u}^{(0)}$, $\mathbf{v}^{(0)}$, $\alpha_1^{(0)}, \alpha_2^{(0)}$ randomly from the prior distribution and choose $\delta_1 \in [0, \infty)$ and $\delta_2 \in [0, 1)$.
2. (MALA) Update $\mathbf{u}$ and α_1:

2.1. Propose $\boldsymbol{\theta}^{(k+1/4)}$ using

$$\mathbf{v}^{(k+1/4)} = \mathbf{v}^{(k)}, \quad \mathbf{w_1} \sim \mathcal{N}(0, \mathbf{P}^{-1}),$$

$$\mathbf{u}^{(k+1/4)} = \frac{2 - \delta_1}{2 + \delta_1}\mathbf{u}^{(k)} - \frac{2\delta_1}{2 + \delta_1}\mathbf{P}^{-1}\nabla_{\mathbf{u}}\Phi\left(\mathbf{a}_h^{(k)}; \mathbf{d}_{\text{obs}}\right) + \frac{\sqrt{8\delta_1}}{2 + \delta_1}\mathbf{w_1},$$

$$\alpha_2^{(k+1/4)} = \alpha_2^{(k)}, \quad \xi_1 \sim \mathcal{N}(0, \sigma_1^2),$$

$$\alpha_1^{(k+1/4)} = \frac{2 - \delta_1}{2 + \delta_1}\alpha_1^{(k)} - \frac{2\delta_1 c_1^2}{2 + \delta_1}\nabla_{\alpha_1}\Phi\left(\mathbf{a}_h^{(k)}; \mathbf{d}_{\text{obs}}\right) + \frac{\sqrt{8\delta_1}}{2 + \delta_1}\xi_1.$$

2.2. Set $\boldsymbol{\theta}^{(k+1/2)} = \boldsymbol{\theta}^{(k+1/4)}$ with probability $\kappa(\boldsymbol{\theta}^{(k)}; \boldsymbol{\theta}^{(k+1/4)})$.

2.3. Otherwise set $\boldsymbol{\theta}^{(k+1/2)} = \boldsymbol{\theta}^{(k)}$.

3. (pCN) Update $\mathbf{v}$ and α_2:

3.1. Propose $\boldsymbol{\theta}^{(k+3/4)}$ using

$$\mathbf{u}^{(k+3/4)} = \mathbf{u}^{(k+1/2)}, \quad \mathbf{w_2} \sim \mathcal{N}(0, \mathbf{P}^{-1}),$$

$$\mathbf{v}^{(k+3/4)} = \sqrt{1 - \delta_2^2}\mathbf{v}^{(k+1/2)} + \mathbf{w_2},$$

$$\alpha_1^{(k+3/4)} = \alpha_1^{(k+1/2)}, \quad \xi_2 \sim \mathcal{N}(0, \sigma_2^2),$$

$$\alpha_2^{(k+3/4)} = \sqrt{1 - \delta_2^2}\alpha_2^{(k+3/4)} + \xi_2.$$

3.2. Set $\boldsymbol{\theta}^{(k+1)} = \boldsymbol{\theta}^{(k+3/4)}$ with probability $\tau(\boldsymbol{\theta}^{(k+1/2)}; \boldsymbol{\theta}^{(k+3/4)})$.

3.3. Otherwise set $\boldsymbol{\theta}^{(k+1)} = \boldsymbol{\theta}^{(k+1/2)}$.

4. Set $k \to k + 1$ and return to step 2.

The acceptance probability in step 2.2 is defined as

$$\kappa(\boldsymbol{\theta}; \tilde{\boldsymbol{\theta}}) := \min\left\{1, \exp\left(\rho(\boldsymbol{\theta}; \tilde{\boldsymbol{\theta}}) - \rho(\tilde{\boldsymbol{\theta}}; \boldsymbol{\theta})\right)\right\} \tag{2.16}$$

where

$$\begin{aligned}
\rho(\boldsymbol{\theta}; \tilde{\boldsymbol{\theta}}) := \Phi(\boldsymbol{\theta}; \mathbf{d}_{\text{obs}}) &+ \frac{1}{2}\begin{bmatrix} \tilde{\alpha}_1 - \alpha_1 \\ h^2(\tilde{\mathbf{u}} - \mathbf{u}) \end{bmatrix}^* \begin{bmatrix} \nabla_{\alpha_1}\Phi(\boldsymbol{\theta}; \mathbf{d}_{\text{obs}}) \\ \nabla_{\mathbf{u}}\Phi(\boldsymbol{\theta}; \mathbf{d}_{\text{obs}}) \end{bmatrix} \\
&+ \frac{\delta}{4}\begin{bmatrix} \tilde{\alpha}_1 + \alpha_1 \\ h^2(\tilde{\mathbf{u}} + \mathbf{u}) \end{bmatrix}^* \begin{bmatrix} \nabla_{\alpha_1}\Phi(\boldsymbol{\theta}; \mathbf{d}_{\text{obs}}) \\ \nabla_{\mathbf{u}}\Phi(\boldsymbol{\theta}; \mathbf{d}_{\text{obs}}) \end{bmatrix} \\
&+ \frac{\delta}{4}\begin{bmatrix} \nabla_{\alpha_1}\Phi(\boldsymbol{\theta}; \mathbf{d}_{\text{obs}}) \\ \nabla_{\mathbf{u}}\Phi(\boldsymbol{\theta}; \mathbf{d}_{\text{obs}}) \end{bmatrix}^* \begin{bmatrix} \sigma_1^2 & 0 \\ 0 & \mathbf{P}^{-1} \end{bmatrix} \begin{bmatrix} \nabla_{\alpha_1}\Phi(\boldsymbol{\theta}; \mathbf{d}_{\text{obs}}) \\ \nabla_{\mathbf{u}}\Phi(\boldsymbol{\theta}; \mathbf{d}_{\text{obs}}) \end{bmatrix}.
\end{aligned} \tag{2.17}$$

The acceptance probability in step 3.2 is

$$\tau(\boldsymbol{\theta}; \tilde{\boldsymbol{\theta}}) := \min\left\{1, \exp\left(\Phi(\boldsymbol{\theta}; \mathbf{d}_{\text{obs}}) - \Phi(\tilde{\boldsymbol{\theta}}; \mathbf{d}_{\text{obs}})\right)\right\}. \tag{2.18}$$

Derivation of the acceptance probabilities is outside the scope of this article and the reader is referred to [9] for details.

Letting $\mathbf{a}_h^{(k)} := \mathbf{a}_h(\boldsymbol{\theta}^{(k)})$, the above algorithm will generate a Markov chain that has the π_{post} as its invariant distribution [37]. This means that the samples can be used to compute

the expected value of functions of the aberrations with respect to π_{post}. Suppose that the expected value of a function f is of interest, then

$$\int f(\mathbf{a})\pi_{\text{post}}(\mathbf{a}|\mathbf{d}_{\text{obs}})d\mathbf{a} \approx \frac{1}{k}\sum_{\ell=1}^{k} f\left(\mathbf{a}_h^{(\ell)}\right). \tag{2.19}$$

The functions of interest for practical applications are the posterior mean $\mathbf{a}_{\text{PM}}$, covariance $\mathbf{Cov}(\mathbf{a})$ and standard deviation $\mathbf{std}(\mathbf{a})$ of the aberration for each element:

$$
\begin{aligned}
\mathbf{a}_{\text{PM}} &\approx \frac{1}{k}\sum_{\ell=1}^{k}\mathbf{Sa}_h^{(\ell)}, \\
\mathbf{Cov}(\mathbf{a}) &\approx \frac{1}{k}\sum_{\ell=1}^{k}(\mathbf{Sa}_h^{(\ell)} - \mathbf{a}_{PM})(\mathbf{Sa}_h^{(\ell)} - \mathbf{a}_{PM})^*, \\
\mathbf{std}(\mathbf{a})_i &\approx (\text{diag}(\mathbf{Cov}(\mathbf{a}))_i)^{1/2} \qquad \text{for} \qquad i = 1, 2, \cdots, N.
\end{aligned} \tag{2.20}
$$

Recall that $\mathbf{S}$ is the discrete approximation of the point-wise evaluation operator S in (2.7) as discussed in Section 2.2.2.

A key detail in implementation of the MwG algorithm is computing the derivative of the likelihood potential in step 2.1. This gradient can be calculated by solving an adjoint problem. Let $\mathbf{G} := \mathbf{FZS}\,\text{diag}(\exp(i\alpha_2^2\mathbf{v}))$ and recall that the pressure field can be written as

$$\mathbf{p} = \mathbf{FZS}\,\text{diag}(\bar{\mathbf{u}} + \alpha_1^2\mathbf{u})\exp(i(\alpha_2^2\mathbf{v})). \tag{2.21}$$

Then, straightforward calculations show that

$$\nabla_{\alpha_1}\mathcal{G}(\boldsymbol{\theta}) = 2\alpha_1\,\text{diag}(\mathbf{p})\mathbf{G}^*\mathbf{u}, \qquad \nabla_{\mathbf{u}}\mathcal{G}(\boldsymbol{\theta}) = 2\alpha_1^2\text{Re}\left[\text{diag}(\mathbf{p})\mathbf{G}^*\right]. \tag{2.22}$$

Combining this with (2.12) gives

$$\begin{bmatrix} \nabla_{\alpha_1}\Phi(\boldsymbol{\theta}; \mathbf{d}_{\text{obs}}) \\ \nabla_{\mathbf{u}}\Phi(\boldsymbol{\theta}; \mathbf{d}_{\text{obs}}) \end{bmatrix} = \begin{bmatrix} \nabla_{\alpha_1}\mathcal{G}(\boldsymbol{\theta})^* \\ \nabla_{\mathbf{u}}\mathcal{G}(\boldsymbol{\theta})^* \end{bmatrix} \boldsymbol{\Sigma}^{-1}(\mathcal{G}(\boldsymbol{\theta}) - \mathbf{d}_{\text{obs}}). \tag{2.23}$$

Therefore, every step of the MALA update costs roughly twice as much as the pCN update but MALA is more efficient in exploring the posterior.

3. Methods. In this section we describe the details of two experiments that were performed to test our framework for estimation of the acoustic aberrations. The first test uses a synthetic dataset which is generated by the same model as the forward model of Section 2.1. In the second test we use a physical dataset that was obtained using a Philips Sonalleve V1 device.

3.1. Test with synthetic displacement map. The first test was performed using a synthetic dataset generated with the target aberrator in Figure 2.1(b). The goal here was to test the algorithm in a more relaxed setting where there was no discrepancy between the forward model and the model for the data.

Generating the synthetic dataset involves many details including the geometry of the transducer and the location of the focal point that are besides the main point of this article. To keep the discussion short, we only present a summary of the methodology for performing the synthetic experiments. The first step in generating the artificial dataset was to identify the free-field matrix of the transducer $\tilde{\mathbf{F}}$ using (2.1) and the location of the elements and the MR-ARFI voxels; The k-th column of $\tilde{\mathbf{F}}$ is simply the free-field corresponding to the k-th element. Afterwards, the matrix $\mathbf{F}$ is constructed using (2.5). The next step was to construct the design matrix $\mathbf{Z}$ which is identified by the $\tilde{\mathbf{z}}_j$ vectors. This matrix contains the prescribed values of the amplitude and phase of the acoustic waves at the emitter. A design matrix was utilized in this example where the virtual elements of [16] were used to group nearby piezoelectric elements. Let $\mathbf{H}_{256}$ denote the 256×256 Hadamard matrix [16, Eq. 8] with columns $\mathbf{h}_1$ to $\mathbf{h}_{256}$. Then $\tilde{\mathbf{z}}_j = \mathbf{h}_1 + \exp(i\frac{\pi}{6})\mathbf{h}_j$ for $j = 2, \cdots, 16$.

A noisy version of the design vectors was considered with

$$\tilde{\mathbf{z}}_j^{\text{noisy}} := \tilde{\mathbf{z}}_j + \boldsymbol{\epsilon}_1 \exp\left(i\frac{\pi}{4}\boldsymbol{\epsilon}_2\right) \quad \text{where} \quad \boldsymbol{\epsilon}_1, \boldsymbol{\epsilon}_2 \sim \mathcal{N}(0, (0.05)^2 \cdot \mathbf{I}_{256\times256}). \qquad (3.1)$$

This added an extra layer of noise that is not accounted for in the formulation of the inverse problem. The standard deviation of the noise in the phase was taken to be 0.05 as a reasonable estimate of the errors in imposing the sonication patterns in practical settings. Putting these vectors together gave a noisy design matrix $\mathbf{Z}^{\text{noisy}}$ and the synthetic dataset was generated using

$$\mathbf{d}_{\text{obs}}^{\text{art}} = \mathbf{F}\mathbf{Z}^{\text{noisy}}\mathbf{a}^{\text{art}} + \boldsymbol{\eta} \quad \text{where} \quad \boldsymbol{\eta} \sim \sigma_{\text{obs}}^{\text{art}} \cdot \mathcal{N}(0, (0.2)^2 \cdot \mathbf{I}_{256\times256}) \qquad (3.2)$$

and $\sigma_{\text{obs}}^{\text{art}}$ is the standard deviation of $\mathbf{F}\mathbf{Z}^{\text{noisy}}\mathbf{a}^{\text{art}}$. The standard deviation of the measurement noise was taken to be 0.2 which implied a signal to noise ration of 5. This choice was made to replicate data that is highly noisy. Figure 3.1 shows examples of the generated noisy data along with the prescribed phase and amplitudes of the elements.

A total of 16 sonication tests were performed in this example, i.e. the design matrix had 16 columns. In order to solve the inverse problem, a coarse 8×8 mesh (i.e. $h = 1/4$) was used to discretize the aberration field a. It was assumed that the noise covariance $\boldsymbol{\Sigma} = (0.15 \cdot \sigma_{\text{obs}}^{\text{art}})^2 \cdot \mathbf{I}_{JM\times JM}$. The prior mean was taken to be $\bar{\mathbf{u}} = 1$, the prior wave number $\gamma = 1/5$ and the hyperparameter prior variances were $\sigma_1 = \sigma_2 = 2$. The step sizes in the MCMC algorithm were $\delta_1 = 4 \times 10^{-5}$ and $\delta_2 = 5 \times 10^{-3}$ resulting in an average acceptance probability of 0.32 across the two Metropolis Hastings updates.

3.2. Test with MR-ARFI displacement map. A test was done using the displacement maps obtained from MR-ARFI data which was acquired using a Philips Sonalleve V1 ultrasound system (Philips Healthcare, Vantaa, Finland) and an Achieva 3T MRI machine (Philips, Best, Netherlands). A phased array transducer consisting of 256 elements was used with a focal length of 12 cm and aperture of 13 cm. The transducer was operating at 1.2 MHz generating ultrasound pulses of 1 ms ranging from 0 to 300 acoustic Watts. The transducer was submerged in an oil tank (as illustrated in Figure 1.1) and the acoustic field was targeted at a 4 cm phantom which mimics muscle tissue (CIRS, Norfolk, VA, USA). The displacement due to the ultrasound pulses was measured using a dedicated MR receiver coil of 4 cm inner diameter. The displacements were measured using MR-ARFI sequences based on a RF-spoiled
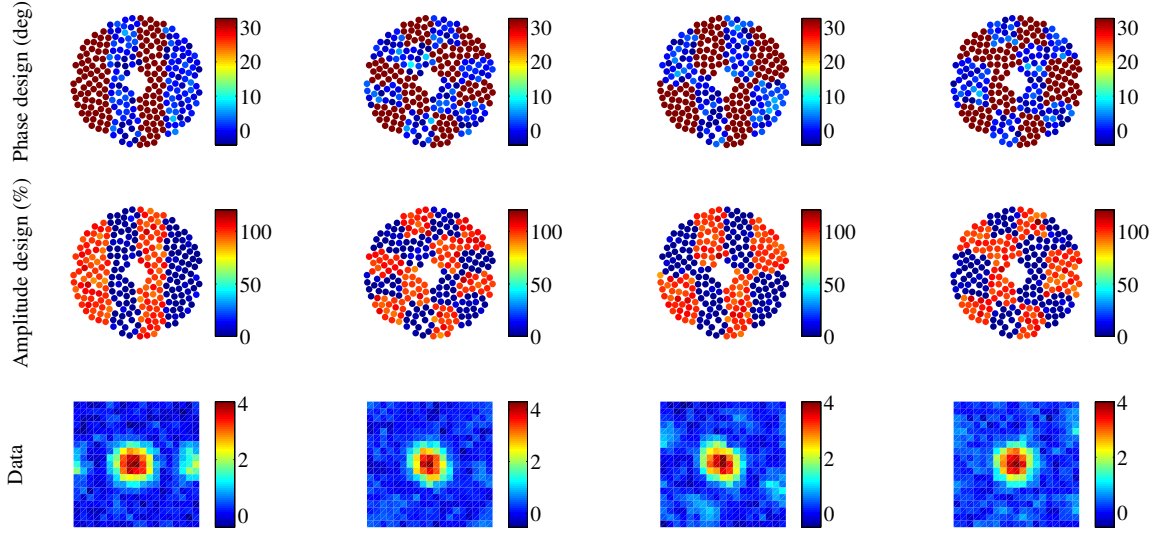
Figure 3.1: A few examples of artificial experiments, indicating the prescribed noisy phase and amplitude (the $\tilde{\mathbf{z}}_j^{\text{noisy}}$ vectors) along with the resulting image of the focal point (subsets of $\mathbf{d}_{\text{obs}}^{\text{art}}$) scaled by the standard deviation of the dataset.

gradient-recalled Echo-Planar Imaging (EPI) sequence with Repetition Time (TR) of 42 ms, Echo Time (TE) of 30 ms, flip angle of 20 degrees, EPI factor of 9, MRI resolution of 64×64 pixels, bi-polar motion encoding gradients of 1 ms in duration and amplitude of 30 mT/m. Images were obtained every 0.26 seconds from a single slice that was orthogonal to the path of the beam with a field of view of 180×180 mm^2 and voxels of size $0.7 \times 0.7 \times 4$ mm^3.

At first, a set of measurements was taken without an aberrator. This dataset is used for estimating the free-field matrix of the transducer and so it is referred to as the calibration dataset. To obtain this dataset the phase stepping technique of [16, 25] was used with 16 virtual elements (the first 16 columns of the Hadamard matrix) with ten steps in phase for each virtual element. Thus, this dataset consists of 160 sonication patterns. A cosine function was then fit to the displacement of each voxel during the phase stepping in order to retrieve the phase and estimate the free-field matrix of each element. A subset of this dataset is used in the calibration step below to further improve the estimate of the free-field matrix.

Afterwards, a second set of measurements was taken in the presence of the aberrator of Figure 2.1(a) consisting of 32 sonication patterns. This dataset is referred to as the reconstruction dataset. The input phase and amplitude of the 256 elements were modified to imitate the effect of the target aberrator instead of using a physical aberrator in front of the beam. That is, the aberrator was added to the prescribed excitation patterns during each sonication test. This approach is advantageous because the values of the aberration parameters are known and so we can easily assess the quality of the estimates. Programming of the HIFU system and collection of MR images were performed using the toolboxes MatHIFU and MatMRI [44]. Here, the design matrix $\mathbf{Z}$ was constructed from the vectors $\tilde{\mathbf{z}}_j = \frac{1}{2}(\mathbf{h}_1 + \mathbf{h}_j)$ for $j = 1, \cdots, 16$

and $\tilde{\mathbf{z}}_j = \frac{1}{2}(\mathbf{h}_1 + \exp(i\frac{\pi}{3}))\mathbf{h}_j)$ for $j = 17, \cdots, 32$. All tests were performed with a field of view of 7×7 voxels, i.e. $\sqrt{M} = 7$. Only a small portion of the images are used from each frame since signal to noise ratio drops rapidly for voxels that are far from the focal point. Each measurement was repeated ten times and then averaged in order to reduce the noise.

The noise covariance in the formulation of the inverse problem was taken to be $\mathbf{\Sigma} = (0.2 \cdot \sigma_{\mathrm{obs}})^2 \cdot \mathbf{I}_{JM \times JM}$ where σ_{obs} is the standard deviation of the reconstruction dataset. Recall that here, $M = 49$ (number of voxels) and $J = 16$ (number of images). As before, an 8×8 grid was used for discretization of the aberration field a. The prior mean was taken to be $\bar{\mathbf{u}} = 1$ and the prior wave number $\gamma = 1/5$. The prior variances on the hyperparameters were $\sigma_1 = 0.5$ and $\sigma_2 = 0.5$ and the MCMC step sizes were $\delta_1 = 1.1 \times 10^{-5}$ and $\delta_2 = 1.5 \times 10^{-3}$ resulting in an average acceptance probability of 0.54 across the two Metropolis Hastings updates.

3.3. Calibration of the free-field matrix. The free-field matrix of the transducer is computed using the phase stepping technique of [16, 25] but the estimated field is often not accurate enough to give a satisfactory estimate of the aberrations. This issue is amplified when measurements are noisy and the number of sonication tests is significantly smaller than the number of elements on the transducer. Furthermore, the MR-ARFI data consists of measurements of displacement while the forward model of Section 2.1 is valid for acoustic intensity. Although acoustic intensity is expected to be proportional to displacement [32], the constant of proportionality is unknown.

These discrepancies will manifest as an apparent aberrator in front of the beam. For example, running the algorithm on the calibration dataset would still estimate a significant value for the aberrations. In practice this aberrator must be estimated in a calibration step before computing the actual aberrator using the reconstruction dataset. This will also automatically estimate the constant of proportionality between intensity and displacement. Here, the posterior mean of this inherent aberrator, denoted by $\mathbf{a}_{\mathrm{calibration}}$, is computed over the first 32 measurements of the calibration dataset. Once this vector is available, the calibration can be performed by simply replacing the matrix $\mathbf{S}$ by

$$\mathbf{S}_{\mathrm{calibrated}} = \mathrm{diag}(\mathbf{a}_{\mathrm{calibration}})\mathbf{S}. \tag{3.3}$$

3.4. Assessing the quality of the refocusing. After assuming that the posterior mean $\mathbf{a}_{\mathrm{PM}}$ is taken to be the best estimator of the true aberration $\mathbf{a}$, take $\boldsymbol{\phi}_{\mathrm{PM}}$ and $\boldsymbol{\phi}$ to be their corresponding phase shifts. Consider the vectors

$$\mathbf{e}_1 := \mathrm{diag}[\tilde{\mathbf{F}}\exp(i(\boldsymbol{\phi} - \boldsymbol{\phi}_{\mathrm{PM}}))]\,\tilde{\mathbf{F}}\exp(i(\boldsymbol{\phi} - \boldsymbol{\phi}_{\mathrm{PM}})),$$
$$\mathbf{e}_2 := \mathrm{diag}[\tilde{\mathbf{F}}\exp(i\boldsymbol{\phi})]\,\tilde{\mathbf{F}}\exp(i\boldsymbol{\phi}),$$
$$\mathbf{e}_3 := \mathrm{diag}[\tilde{\mathbf{F}}\mathbf{1}]\,\tilde{\mathbf{F}}\mathbf{1}.$$

Now the expected improvement functional EI and the expected recovery functional ER for the posterior mean are defined as

$$EI(\mathbf{a}_{\mathrm{PM}}) := \left(1 - \frac{\|\mathbf{e}_3\|_\infty - \|\mathbf{e}_1\|_\infty}{\|\mathbf{e}_3\|_\infty - \|\mathbf{e}_2\|_\infty}\right) \times 100, \quad ER(\mathbf{a}_{\mathrm{PM}}) := \left(\frac{\|\mathbf{e}_1\|_\infty - \|\mathbf{e}_2\|_\infty}{\|\mathbf{e}_3\|_\infty}\right) \times 100.$$

EI measures the percentage of lost intensity that is recovered while ER measures how the maximum intensity of the refocused beam compares to the the maximum intensity of a perfectly focused beam. These measures are used in the next section in order to further assess the performance of the estimates for the three tests that were discussed above.

4. Results.

4.1. Test with synthetic displacement map.
A summary of Bayesian posterior statistics using the synthetic dataset is presented in Figure 4.1. Posterior mean and standard deviations are computed using 5×10^5 samples with a burn-in period of 3×10^3 samples (i.e. the first 3×10^3 samples were discarded since the Markov chain had not yet converged at that point). The posterior mean (Figure 4.1(b)) is taken to be a good estimator of the actual value of the parameters. This is supported by Figure 4.1(c) which is the point-wise absolute difference between the posterior mean and the target aberrator. Here the maximum error in the phase is 21 degrees while the average error (among the elements) is 4.5 degrees. As for the attenuation, the maximum error is 45 percent and the average error is 14 percent. Compare these values to Figure 4.1(d) which depicts the standard deviation of the aberration parameters and can be taken as a measure of uncertainty in the approximations. The standard deviation of the aberrations is close the the average point wise absolute error. Therefore, the standard deviation is a good measure of the accuracy of $\mathbf{a}_{\mathrm{PM}}$. Furthermore, Figure 4.1(f) compares the prediction of the data using $\mathbf{a}_{\mathrm{PM}}$ to the actual data set on a few frames of the MR-ARFI data. This shows a good agreement between the prediction and the data and further certifies the choice of $\mathbf{a}_{\mathrm{PM}}$ as a point-wise estimator of the target. Finally, for the expected improvement $EI(\mathbf{a}_{\mathrm{PM}}) \approx 71\%$ and $ER(\mathbf{a}_{\mathrm{PM}}) \approx 5\%$. Therefore, using $\mathbf{a}_{\mathrm{PM}}$ to refocus the beam recovers 71% of the lost intensity. However, this only improves maximum intensity by 5% which is due to the fact that the aberrator of Figure 4.1(a) is very weak and the defocused beam is already at 93% intensity.

In the case of the hyperparameters, one can integrate out the rest of the parameters and directly estimate the marginal posterior distribution as in Figure 4.1(e). These results indicate a drop of two orders of magnitude in the standard deviation of the hyperparameters, compared with the prior standard deviation, indicating that the value of the hyperparameters are computed with high confidence.

In addition to the above statistics, one can also look at independent samples from π_{post} as depicted in Figure 4.2. These samples are generated by choosing individual samples from the Markov chain that are far enough apart. The distance between the samples in Figure 4.2 was chosen large enough so that the integrated autocorrelation function of the chain was below 10^{-3}. In this case the distance was taken to be 10^5 steps based on the worst integrated autocorrelation function in Figure 5.1(a). The independent samples can be taken as examples of aberrators that are likely to have generated the dataset and provide further insight regarding π_{post}. It is clear that the samples have very similar features in comparison to the mean. For example, there are no discontinuities or multi-modal behavior. This further supports the choice of the posterior mean $\mathbf{a}_{\mathrm{PM}}$ as a point estimator for the true value of the parameters.

4.2. Test with MR-ARFI displacement map.
Figures 8 to 10 show a similar summary of the results for the test with MR-ARFI displacement map as was shown for the test with
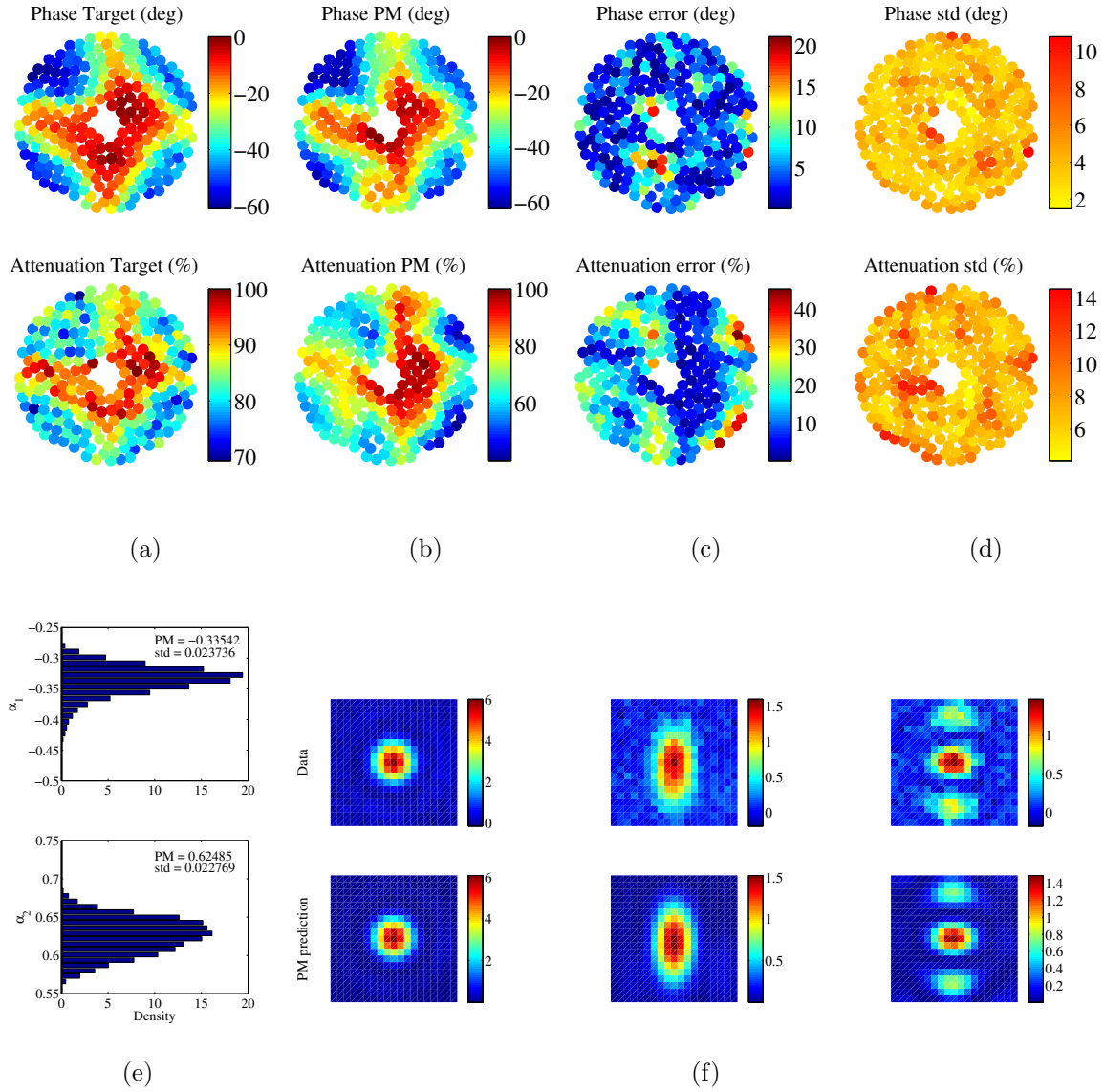
Figure 4.1: A summary of Bayesian posterior statistics using the synthetic dataset. (a) The target aberrator used for generating the data. (b) Posterior mean (PM) of the aberration parameters along with (c) the point-wise difference between the posterior mean and the target aberrator. (d) The standard deviation (std) of the posterior samples which is indicative of the level of uncertainty. (e) Estimated marginal posterior distributions on the hyperparameters. (f) A few examples of the predicted data using the posterior mean in comparison to the synthetic dataset.
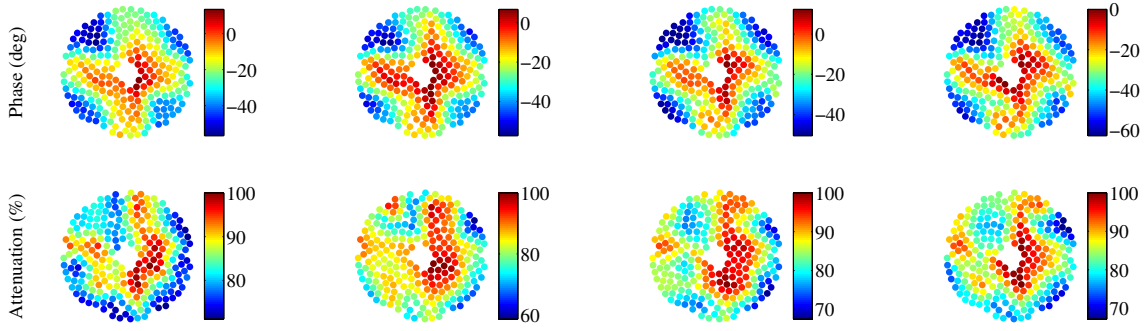
Figure 4.2: A few samples from π_{post} on the aberration parameters. The samples are 10^5 steps apart in the Markov chain so that they can be treated as independent.

synthetic displacement maps. Here the results were computed using 5×10^5 samples from the Markov chain with a burn-in period of 3×10^5. Figure 4.3(b) shows the posterior mean $\mathbf{a}_{\text{PM}}$ which is once again taken to be a good estimator of the aberration parameters. Figure 4.3(c) depicts the point-wise absolute error between $\mathbf{a}_{\text{PM}}$ and the target. Here, the maximum error in the phase is 45 degrees and the average error across the elements is 19 degrees. The maximum error in the amplitude is 30% and the averaged error is 14%. The errors here are notably larger as compared to the test with the synthetic displacement map, especially in the case of the attenuation. This is most likely due to large discrepancies between the forward model and the measured MR-ARFI data. Nevertheless, the overall shape of the aberrator and range of phase shifts are captured even with such a small dataset.

Figure 4.3(d) shows an estimate of the standard deviation of the aberrations under π_{post} indicating a possible error of plus or minus 12 degrees. It should be noted that this error is still smaller than the true point-wise error and the algorithm underestimate the true uncertainty of the solution. Figure 4.3(e) shows the posterior marginal on the hyperparameters. As before, the posterior standard deviation on the hyperparameters has been reduced significantly as compared to that of the prior distribution which is a sign that these parameters are well identified by the data. To check whether the prediction of $\mathbf{a}_{\text{PM}}$ matches the data, a few frames of the MR-ARFI images are compared to the prediction at the posterior mean in Figure 4.3(f). The matching between the data and the prediction was adequate at the focal point but deteriorates away from it. Specifically, the prediction obtained the correct range of variations of each frame and the right location for the point of maximum intensity.

For this dataset $EI(\mathbf{a}_{\text{PM}}) \approx 42\%$ which predicts a good recovery of the intensity. However, expected recovery $ER(\mathbf{a}_{\text{PM}}) \approx 3\%$ which is smaller in comparison to the synthetic test above. This is expected since the estimate of the aberrator is no as accurate as before due to discrepancies between the model and the physical data.

Finally, a few independent samples from π_{post} are presented in Figure 4.4. The samples are 10^5 steps apart in order to ensure their independence. This choice was based on the slowest decaying integrated autocorrelation function in Figure 5.1(b). Once again, comparing the samples to the posterior mean indicates that the samples are close to the posterior mean

and so $\mathbf{a}_{PM}$ is a reasonable point estimator for the parameter values.
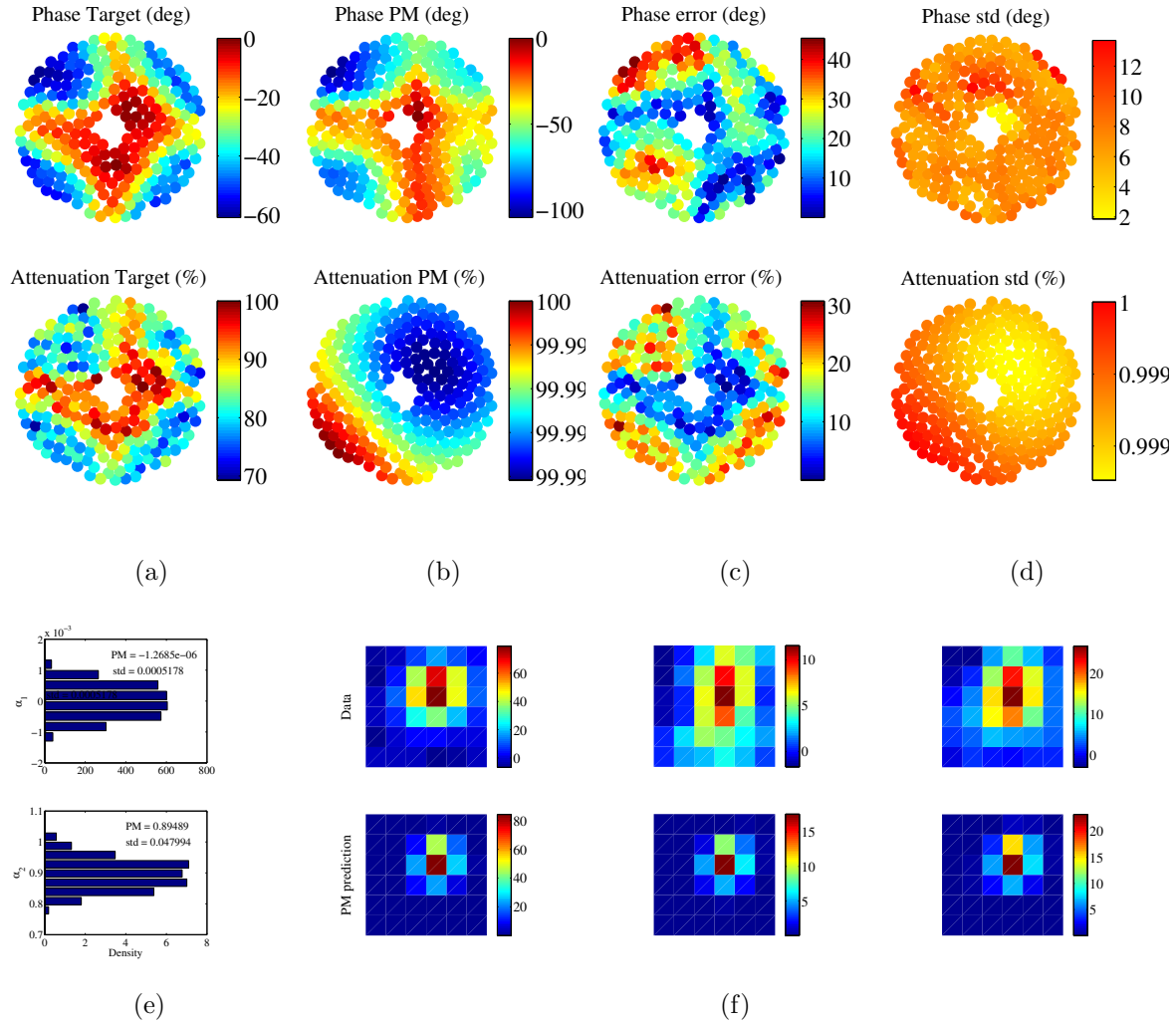

Figure 4.3: A summary of Bayesian posterior statistics using the experimental MR-ARFI dataset. (a) The target aberrator imposed on the transducer. (b) The posterior mean ($\mathbf{a}_{PM}$) and (c) point-wise difference between the posterior mean and the target aberrator. (d) The standard deviation of the posterior. (e) The marginal distribution of the hyperparameters estimated using the Markov chain. (f) A comparison between a few frames of the MR-ARFI data and the prediction of the forward model at the posterior mean.

5. Discussion.

5.1. Mathematical framework.
The most notable feature of the forward problem in (2.6) is that $\mathbf{d}$ is a non-linear function of the aberration $\mathbf{a}$. This is an attribute of the MR-ARFI
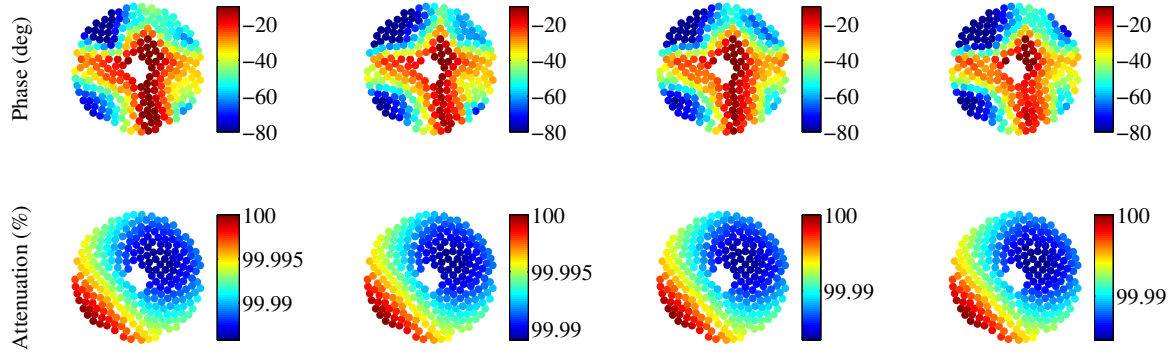
Figure 4.4: Four samples from the Markov chain after converging to the posterior distribution with the experimental MR-ARFI dataset. The samples are 10^5 steps apart so that they can be treated as independent.

data which makes the inverse problem more challenging to solve. In particular, this means that one-shot methods for computing the minimizers of regularized least squares functionals (such as the common Tikhonov regularization) are no longer applicable. In this case one can use numerical optimization algorithms such as Newton's method or the L-BFGS algorithm [42, 34] to find a minimizer but this choice requires a modification of the formulation to get around the non-differentiability of the forward map with respect to the phase. Also, the optimization framework does not provide an estimate of the uncertainty on the parameters and hyperparameters nor does it generate samples from π_{post}.

The presented formulation of the forward and inverse problems together offer complete freedom in the choice of the number of sonications tests J, the size of the MRI images M, the size of the parameter space for the aberrations G and the number of elements N. In practice, it is preferable to take J to be as small as possible to reduce the time required to collect the MRI data. It is also desirable to choose G to be small in order to reduce the computational cost of the algorithms. Taking M to be large means that each MRI image will have more information. However, the signal to noise ratio drops rapidly for voxels that are far from the focal point. This is the main reason why the dataset in the MR-ARFI experiments uses a much smaller field of view compared with the artificial example. Then the choice of each one of these parameters is a delicate task that requires further study in future.

5.2. Performance of the MCMC algorithm. The pCN algorithm is a modification of the random walk Metropolis Hastings algorithm that is well defined on a function space [9]. It tends to generate samples that are highly correlated and so it explores the posterior distribution slowly. However, the pCN update does not require derivative information and therefore can be used to sample from non-differentiable densities. This also means that each step of pCN is relatively inexpensive. The MALA algorithm utilizes an optimal proposal step that results in less correlated samples [37, 9] which makes the algorithm better at exploring the posterior distribution π_{post} but each step of the algorithm has a higher computational

cost. This cost becomes significant when a large dataset is at hand, because this increases the cost of gradient computations.

The difference between the two steps of the algorithm is apparent in Figure 5.1(a) where the integrated autocorrelation functions and trace plots are presented for the likelihood potential Φ and the two hyperparameters α_1 and α_2 in the test with synthetic dataset. The integrated autocorrelation of α_2 decays slower as compared to that of α_1. This is because samples from the latter are generated using the MALA updates. The α_2 chain is slow because in this case the data is fairly informative in the direction of phase, meaning that the posterior distribution π_{post} is dominated by the likelihood rather than the prior distribution. Looking at the trace plots in Figure 5.1 , it is interesting that the Φ chain demonstrates better mixing in comparison to the chains for α_1 and α_2.

Looking at Figure 5.1(b) we notice that the algorithm is behaving quite differently for the physical dataset. The most obvious difference is in the chain for α_1 which is highly uncorrelated. The main reason behind this behavior is that the phase stepping technique [16, 25] that is used to retrieve the displacement maps rescales the MR-ARFI data and loses the information on the attenuation. In other words, the data is not informative in the direction of attenuation and so the marginal posterior on α_1 is very similar to the prior. As for α_2 we notice that the autocorrelation function is decaying slightly faster in comparison to Figure 5.1(a) and the trace plot also indicates better mixing.

The results of this article were obtained using an implementation of the MwG algorithm for estimation of the aberrator in MATLAB on a personal laptop (MacBook Pro with a 3GHz Intel Core i7 processor and 8 GB or memory) in less than two hours. This processing time may not be ideal for practical settings but it can be effectively reduced by implementation of the algorithm in C/C++ and applying techniques such as parallel tempering and population MCMC [28] to further reduce the required sample size needed to compute the expectations.

5.3. Quality of the estimates with synthetic and physical datasets. In Section 4.1 the results with a synthetic dataset were presented. This example is viewed as an idealized setting where there is little discrepancy between the process for generation of the data and the forward model. The results showed that the reconstructions were adequate even in the presence of large errors, the posterior mean $\mathbf{a}_{\mathrm{PM}}$ of the phase (Figure 4.1(b)) was very close to the actual value of the aberrations (the average point-wise error of the phase estimate was 4.5 degrees which amounts to 15% relative error). Furthermore, the estimated standard deviation appeared to be a good estimate of the expected errors in the reconstruction. However, in the case of the attenuation, the posterior mean $\mathbf{a}_{\mathrm{PM}}$ was not as accurate as the phase shift even in this idealized setting (compare Figure 4.1(a) and (b)) . This was due to the fact that the displacement data was not sensitive to relatively small changes in the attenuation.

A more severe case of the issue with the estimation of the attenuation was shown with the experimental dataset with MR-ARFI displacement maps. In this case, the discrepancy between the model and the physical data as well as the normalizing step of the phase stepping technique of [16, 25] made it impossible to estimate the attenuation. Consequently, the resulting posterior distribution π_{post} on the attenuation (Figure 4.3(b)) was essentially the prior with a different variance. Nonetheless, estimation of the attenuation from experimental data remains a challenge within our framework. However, this is not a significant drawback
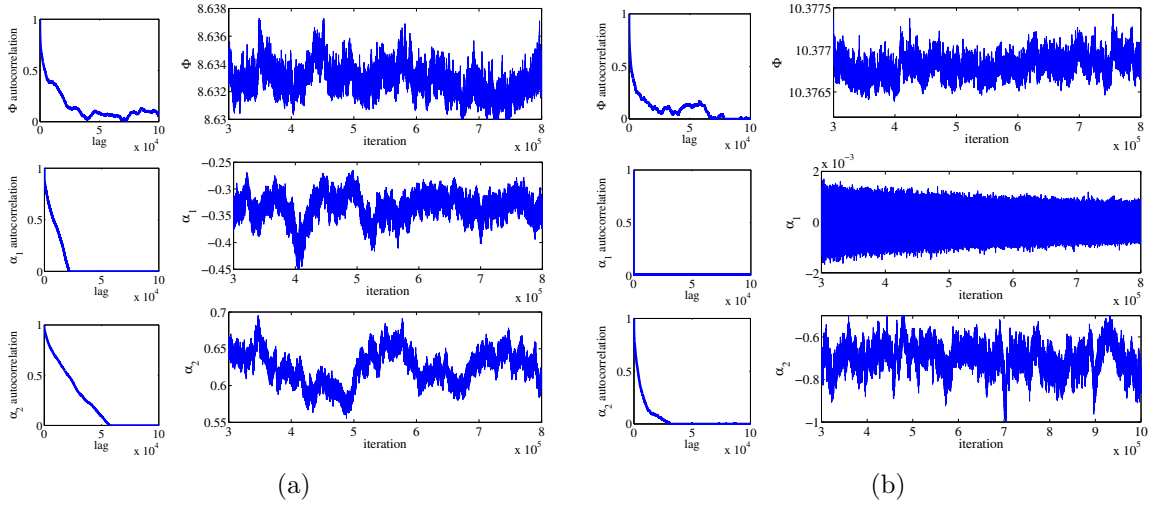
Figure 5.1: Autocorrelation and trace plots of the likelihood potential and hyperparameters using (a) the synthetic dataset and (b) the experimental MR-ARFI displacement map.

as the attenuations have a minor effect on the focusing of the beam compared with the phase shift.

It should be noted that estimating the free-field matrix and the calibration step can both be done at a different time before performing experimenting with the presence of an aberrator. Then, the processing time for the 160 sonication patterns of the calibration dataset are not a major restriction during a real *in vivo* experiment or future clinic treatment. The primary objective is to reduce the size of the reconstruction dataset as much as possible.

The computed free-field matrix of the transducer and the calibration step have a significant impact on the quality of the reconstructions. In the test with experimental MR-ARFI displacement map of Section 4.2 the free-field was estimated using 160 sonication tests with ten steps in phase for each virtual elements. Using subsets of this data resulted in a less accurate free-field matrix which in turn resulted in very different reconstructions. Then one might prefer to use a large dataset in order to obtain an accurate estimate of the free-field matrix which can be used on a smaller reconstruction dataset later on.

5.4. Future research. The framework presented in this article can be extended in multiple directions in order to improve the quality of the reconstructions which, in turn, will lead to better focusing of the beam. Obtaining an accurate estimate of the empirical free-field with the minimum number of sonication tests is a crucial task. The estimates of the aberrations become more sensitive to the free-field matrix as the dataset becomes smaller. Therefore, a good estimate of the free-field matrix is needed in order to further reduce the number sonication tests that are performed under *in vivo* or clinic conditions. In [29] the authors argue that the free-field matrix is often low rank or at least it has fast decaying singular values. This suggests that ideas from the Compressive Sensing and Matrix Completion literature on recovery of low rank matrices [15] are applicable here. This approach has been applied successfully for solution

of the phase retrieval problem [5, 6] which is closely related to the problem at hand.

Another promising direction for future research is improving the sampling algorithm. MCMC algorithms often have a difficult time traversing high dimensional distributions. In such cases, strategies such as population or adaptive MCMC or parallel tempering [28] can be used to improve the statistical performance of the chain. Alternatively, one can also improve the algorithm by changing the forward model so that it is differentiable in the phase. This would allow the use of the MALA update on the entire posterior which would greatly improve the performance.

On the topic of MR-ARFI experiments, one can explore multiple directions for improving the quality of the dataset. An interesting question is the interplay between voxel size, measurement noise and acquisition duration. Smaller voxels give a better estimate of the free-field matrix and the aberration but they are associated with more noise. This, in turn, requires smaller phase steps and longer acquisition time or perhaps more averaging steps per sonication test. Therefore, finding the optimal parameters for generating the dataset remains a challenge in practice.

REFERENCES

[1] S. Agapiou, J. M. Bardsley, O. Papaspiliopoulos, and A. M. Stuart. Analysis of the Gibbs sampler for hierarchical inverse problems. *SIAM/ASA Journal on Uncertainty Quantification*, 2(1):511–544, 2014.

[2] S. Arridge, J. Kaipio, V. Kolehmainen, M. Schweiger, E. Somersalo, T. Tarvainen, and M. Vauhkonen. Approximation errors and model reduction with an application in optical diffusion tomography. *Inverse Problems*, 22:175–195, 2006.

[3] J. F. Aubry, M. Tanter, M. Pernot, J. L. Thomas, and M. Fink. Experimental demonstration of noninvasive transskull adaptive focusing based on prior computed tomography scans. *The Journal of the Acoustical Society of America*, 113(1):84–93, 2003.

[4] D. Calvetti and E. Somersalo. *An Introduction to Bayesian Scientific Computing: Ten Lectures on Subjective Computing*, volume 2. Springer Science and Business Media, New York, 2007.

[5] E. J. Cándes, Y. C. Eldar, T. Strohmer, and V. Voroninski. Phase retrieval via matrix completion. *SIAM Review*, 57(2):225–251, 2015.

[6] E. J. Ćandes, T. Strohmer, and V. Voroninski. Phaselift: Exact and stable signal recovery from magnitude measurements via convex programming. *Communications on Pure and Applied Mathematics*, 66(8):1241–1274, 2013.

[7] J. Chen, R. Watkins, and K. B. Pauly. Optimization of encoding gradients for MR-ARFI. *Magnetic Resonance in Medicine*, 63(4):1050–1058, 2010.

[8] E. Constanciel Colas, A. C. Waspe, C. Mougenot, T. Looi, S. Pichardo, and J. M. Drake. Mapping of insertion losses and time-of-flight delays of pediatric skulls using a clinical MR-guided high intensity focused ultrasound system. In *International Society for Therapeutic Ultrasound*, Utrecht, Netherlands, April 2015.

[9] S. L. Cotter, G. O. Roberts, A. M. Stuart, and D. White. MCMC methods for functions: modifying old algorithms to make them faster. *Statistical Science*, 28(3):424–446, 2013.

[10] S. Crouzet, F. J. Murat, G. Pasticier, P. Cassier, J. Y. Chapelon, and A. Gelet. High intensity focused ultrasound (HIFU) for prostate cancer: current clinical status, outcomes and future perspectives. *International Journal of Hyperthermia*, 26(8):796–803, 2010.

[11] T. Cui, C. Fox, and M. J. O'Sullivan. Bayesian calibration of a large-scale geothermal reservoir model by a new adaptive delayed acceptance Metropolis Hastings algorithm. *Water Resources Research*, 47(10), 2011.

[12] M. C. Edwards, R. Meyer, and N. Christensen. Bayesian parameter estimation of core collapse supernovae using gravitational wave simulations. *Inverse Problems*, 30(11):114008, 2014.

[13] W. J. Elias, D. Huss, T. Voss, J. Loomba, M. Khaled, E. Zadicario, R. C. Frysinger, S. A. Sperling, S. Wylie, S. J. Monteith, et al. A pilot study of focused ultrasound thalamotomy for essential tremor. *New England Journal of Medicine*, 369(7):640–648, 2013.

[14] F. M. Fennessy and C. M. Tempany. A review of magnetic resonance imaging-guided focused ultrasound surgery of uterine fibroids. *Topics in Magnetic Resonance Imaging*, 17(3):173–179, 2006.

[15] S. Foucart and H. Rauhut. *A mathematical introduction to compressive sensing.* Springer Science and Business Media, New York, 2013.

[16] E. Herbert, M. Pernot, G. Montaldo, M. Fink, and M. Tanter. Energy-based adaptive focusing of waves: application to noninvasive aberration correction of ultrasonic wavefields. *IEEE Transactions on Ultrasonics, Ferroelectrics and Frequency Control*, 56(11):2388–2399, 2009.

[17] K. Hynynen and J. Sun. Trans-skull ultrasound therapy: The feasibility of using image-derived skull thickness information to correct the phase distortion. *IEEE Transactions on Ultrasonics, Ferroelectrics, and Frequency Control*, 46(3):752–755, 1999.

[18] M. A. Iglesias, K. Lin, and A. M. Stuart. Well-posed Bayesian geometric inverse problems arising in subsurface flow. *Inverse Problems*, 30(11):114001, 2014.

[19] M. E. Ikink, M. J. Voogt, H. M. Verkooijen, P. N. Lohle, K. J. Schweitzer, A. Franx, P. T. M. Willem, L. W. Bartels, and M. A. van den Bosch. Mid-term clinical efficacy of a volumetric magnetic resonance-guided high-intensity focused ultrasound technique for treatment of symptomatic uterine fibroids. *European Radiology*, 23(11):3054–3061, 2013.

[20] R. Illing, J. Kennedy, F. Wu, G. Ter Haar, A. Protheroe, P. Friend, F. Gleeson, D. Cranston, R. Phillips, and M. Middleton. The safety and feasibility of extracorporeal high-intensity focused ultrasound (HIFU) for the treatment of liver and kidney tumours in a western population. *British Journal of Cancer*, 93(8):890–895, 2005.

[21] D. Jeanmonod, B. Werner, A. Morel, L. Michels, E. Zadicario, G. Schiff, and E. Martin. Transcranial magnetic resonance imaging–guided focused ultrasound: noninvasive central lateral thalamotomy for chronic neuropathic pain. *Neurosurgical Focus*, 32(1):E1, 2012.

[22] J. Kaipio and E. Somersalo. *Statistical and Computational Inverse Problems.* Springer Science and Business Media, New York, 2005.

[23] J. P. Kaipio, V. Kolehmainen, E. Somersalo, and M. Vauhkonen. Statistical inversion and Monte Carlo sampling methods in electrical impedance tomography. *Inverse Problems*, 16(5):1487, 2000.

[24] E. A. Kaye, Y. Hertzberg, M. Marx, B. Werner, G. Navon, M. Levoy, and K. B. Pauly. Application of Zernike polynomials towards accelerated adaptive focusing of transcranial high intensity focused ultrasound. *Medical Physics*, 39(10):6254–6263, 2012.

[25] B. Larrat, M. Pernot, G. Montaldo, M. Fink, and M. Tanter. Mr-guided adaptive focusing of ultrasound. *IEEE Transactions on Ultrasonics, Ferroelectrics, and Frequency Control*, 57(8):1734–1747, 2010.

[26] B. Liberman, D. Gianfelice, Y. Inbar, A. Beck, T. Rabin, N. Shabshin, G. Chander, S. Hengst, R. Pfeffer, A. Chechick, et al. Pain palliation in patients with bone metastases using MR-guided focused ultrasound surgery: a multicenter study. *Annals of Surgical Oncology*, 16(1):140–146, 2009.

[27] N. Lipsman, M. L. Schwartz, Y. Huang, L. Lee, T. Sankar, M. Chapman, K. Hynynen, and A. M. Lozano. MR-guided focused ultrasound thalamotomy for essential tremor: a proof-of-concept study. *The Lancet Neurology*, 12(5):462–468, 2013.

[28] J. S. Liu. *Monte Carlo Strategies in Scientific Computing.* Springer Series in Statistics. Springer, 2008.

[29] N. Liu, A. Liutkus, J.-F. Aubry, L. Marsac, M. Tanter, and L. Daudet. Random calibration for accelerating MR-ARFI guided ultrasonic focusing in transcranial therapy. *Physics in Medicine and Biology*, 60(3):1069, 2015.

[30] F. Marquet, M. Pernot, J. F. Aubry, G. Montaldo, L. Marsac, M. Tanter, and M. Fink. Non-invasive transcranial ultrasound therapy based on a 3D CT scan: protocol validation and in vitro results. *Physics in Medicine and Biology*, 54(9):2597, 2009.

[31] L. Marsac, D. Chauvet, B. Larrat, M. Pernot, B. Robert, M. Fink, A.-L. Boch, J.-F. Aubry, and M. Tanter.

MR-guided adaptive focusing of therapeutic ultrasound beams in the human head. *Medical Physics*, 39(2):1141–1149, 2012.

[32] N. McDannold and S. E. Maier. Magnetic resonance acoustic radiation force imaging. *Medical Physics*, 35(8):3748–3758, 2008.

[33] E. Niemi, M. Lassas, and S. Siltanen. Dynamic x-ray tomography with multiple sources. In *8th International Symposium on Image and Signal Processing and Analysis (ISPA)*, pages 618–621. IEEE, 2013.

[34] J. Nocedal and S. J. Wright. *Numerical Optimization*. Springer, 2nd edition, 2006.

[35] S. Pursiainen and M. Kaasalainen. Sparse source travel-time tomography of a laboratory target: accuracy and robustness of anomaly detection. *Inverse Problems*, 30(11):114016, 2014.

[36] J. W. S. Rayleigh. *The theory of sound*. Dover, New York, 1945.

[37] C. Robert and G. Casella. *Monte Carlo statistical methods*. Springer Science and Business Media, New York, 2013.

[38] E. A. Stewart, J. Rabinovici, C. M. Tempany, Y. Inbar, L. Regan, B. Gastout, G. Hesley, H. S. Kim, S. Hengst, and W. M. Gedroye. Clinical outcomes of focused ultrasound surgery for the treatment of uterine fibroids. *Fertility and Sterility*, 85(1):22–29, 2006.

[39] A. M. Stuart. Inverse problems: a Bayesian perspective. *Acta Numerica*, 19:451–559, 2010.

[40] A. Tarantola. *Inverse Problem Theory and Methods for Model Parameter Estimation*. SIAM, 2005.

[41] G. ter Haar and C. Coussios. High intensity focused ultrasound: physical principles and devices. *International Journal of Hyperthermia*, 23(2):89–104, 2007.

[42] C. R. Vogel. *Computational Methods for Inverse Problems*. SIAM, 2002.

[43] F. Wu, Z.-B. Wang, W.-Z. Chen, W. Wang, Y. Gui, M. Zhang, G. Zheng, Y. Zhou, G. Xu, M. Li, et al. Extracorporeal high intensity focused ultrasound ablation in the treatment of 1038 patients with solid carcinomas in China: an overview. *Ultrasonics Sonochemistry*, 11(3):149–154, 2004.

[44] B. Zaporzan, A. C. Waspe, T. Looi, C. Mougenot, A. Partanen, and S. Pichardo. MatMRI and MatHIFU: software toolboxes for real-time monitoring and control of MR-guided HIFU. *Journal of Therapeutic Ultrasound*, 1(1):1–12, 2013.